

Closed-Cage Tungsten Oxide Clusters in the Gas Phase

D. M. David Jeba Singh,^{†,‡} T. Pradeep,^{*,†} Krishnan Thirumoorthy,[‡] and Krishnan Balasubramanian^{*,‡,§,||}

DST Unit on Nanoscience, Department of Chemistry and Sophisticated Analytical Instrument Facility, Indian Institute of Technology Madras, Chennai 600 036, India, College of Science, California State University, East Bay, Hayward, California 94542, Chemistry and Material Science Directorate, Lawrence Livermore National Laboratory, P.O. Box 808 L-268, Livermore, California 94550, and Lawrence Berkeley Laboratory, University of California, Berkeley, California 94720

Received: December 17, 2009; Revised Manuscript Received: March 19, 2010

During the course of a study on the clustering of W–Se and W–S mixtures in the gas phase using laser desorption ionization (LDI) mass spectrometry, we observed several anionic W–O clusters. Three distinct species, $W_6O_{19}^-$, $W_{13}O_{29}^-$, and $W_{14}O_{32}^-$, stand out as intense peaks in the regular mass spectral pattern of tungsten oxide clusters suggesting unusual stabilities for them. Moreover, these clusters do not fragment in the postsource decay analysis. While trying to understand the precursor material, which produced these clusters, we found the presence of nanoscale forms of tungsten oxide. The structure and thermodynamic parameters of tungsten clusters have been explored using relativistic quantum chemical methods. Our computed results of atomization energy are consistent with the observed LDI mass spectra. The computational results suggest that the clusters observed have closed-cage structure. These distinct W_{13} and W_{14} clusters were observed for the first time in the gas phase.

1. Introduction

In recent years, closed-cage clusters in the gas phase have attracted the attention of many researchers.^{1,2} Studies of clusters in the gas phase give qualitative information about their structure and stability, especially as a function of size. Such data would be helpful to study their reactivity and catalytic activity. Mass spectrometer is an ideal tool to study the formation of closed-cage clusters in the gas phase as it provides vital information on relative abundances as a function of cluster size. Some of the methods to generate clusters in the gas phase are vaporization, ion bombardment, and laser desorption. Computations along with experiments give a comprehensive understanding of the clusters.

Clusters comprised of certain number of atoms known as magic numbers exhibit enhanced stability over other clusters. As the mass spectrometry of clusters is vast, we point out only a few relevant reports here. Reviews on various aspects of cluster science may be consulted for a detailed discussion.³ Magic number clusters showing enhanced stability have been reported for Si_{13} ⁴ and Al_{13} .⁵ Whereas mass selected positively charged Si_{13} clusters were completely unreactive to both ethylene and NO, Si clusters with other nuclearities react. The Al_{13} cluster does not show any reactivity with oxygen, while other neighboring clusters did. Structure and reactivity of specific Al clusters such as Al_{12} , Al_{16} , Al_{17} , and Al_{18} have been extensively explored by Castleman and Khanna.⁶ Magic-numbered silver clusters formed by matrix-assisted laser desorption mass spectrometry

were reported by Kéki et al.⁷ Apart from monometallic clusters, they also reported bimetallic Ag–Au clusters.⁸ Many kinds of transition metal oxide clusters have been explored in the gas phase.^{9–11} The structure of vanadium cage clusters has been studied by Asmis and Sauer using gas phase infrared spectroscopy.¹² Magic-numbered water clusters with dodecahedral structure were reported by Searcy and Fenn.¹³ Various cage clusters have been reported in the condensed phase as well. Clusters comprised of Zr_{12} as the closed cage with various transition metals in the interstitial site were reported by Yang et al.¹⁴ Clusters having nine vertices composed of three molybdenum, four sulfur, and two carbon atoms have been reported by Ide and Shibahara in 2004.¹⁵ Bridgeman and Cavigliasso investigated the structure and bonding in $[W_{10}O_{32}]^{n-}$ isopolyanions theoretically.¹⁶ Various kinds of metal–carbon cage clusters were explored in great detail by Guo et al.¹⁷ Molecular level details of small WO clusters on oxidative catalysis have been reported by Johnson et al.¹⁸ recently. Rothgeb et al.¹⁹ reported the unusual reactivity of small anionic WO clusters with H_2O and D_2O .

A cluster of formula $Mo_{13}S_{25}$, showing high stability over neighboring clusters, was reported by some of us recently.²⁰ A larger Mo_{14} cluster with a molybdenum atom inside has also been observed.²¹ These closed-cage clusters were suggested to be formed by curling up of nanoflakes of molybdenum sulphide upon laser irradiation. For oxide clusters, a structural changeover occurred near Mo_8 clusters.²² Clusters formed from WO_3 and H_2WO_4 were also reported. A mixture of elements like Te and S in the condensed phase forms molecular clusters of TeS in the gas phase.²³ These examples imply numerous possibilities to study similar clusters in the gas phase. Magic-numbered metal and metal oxide clusters are important because of their physical and chemical properties in comparison to the bulk materials. Several such novel materials have been synthesized in the bulk, once they were studied systematically in the gas phase. A

* To whom correspondence should be addressed. (T.P.) E-mail: pradeep@iitm.ac.in. Fax: + +91 44 22570509/0545. (K.B.) E-mail: balu@llnl.gov. Fax: 001-925-422-6810.

[†] Indian Institute of Technology Madras.

[‡] California State University.

[§] Lawrence Livermore National Laboratory.

^{||} University of California.

[–] Currently at Department of Chemistry, Penn State University, University Park, PA 16802.

famous example is C_{60} .²⁴ Mass selected WO showed characteristic reactivity in the cracking of hydrocarbons.¹⁸ Magic-numbered clusters such as W_{13} and W_{14} oxides may show unprecedented reactivity over other clusters. Very few reports exist on inorganic closed-cage clusters in the gas phase.

In this work, we have presented the results on the formation of negatively charged W–O clusters in the gas phase. These anionic clusters were observed during our attempt to study the clustering of W–Se and W–S mixtures. The observed clusters, $W_6O_{19}^-$, $W_{13}O_{29}^-$, and $W_{14}O_{32}^-$ are especially stable and exhibit much larger relative abundances compared to the neighboring clusters. We have performed relativistic quantum chemical calculations to understand the structure and stabilities of these clusters as a function of their sizes and also to interpret the observed LDI mass spectra. Our theoretical results support the observed stabilities of the magic-numbered clusters in the gas phase. We note that while most of our previous gas phase work was on sulphides,^{20,21} the present work is on oxides. The precursors used for the present studies are also different.

2. Experimental Methods

Chemicals used in this study were purchased from Aldrich and were used without further purification. We have chosen ball-milling to prepare a stoichiometric mixture of W + Se and W + S from elemental tungsten, selenium, and sulfur. Corresponding elements in 1:2 molar ratios were mixed and ball milled with a Retsch planetary ball mill (PM 200) for about 1 h. The resultant material was further studied by laser desorption mass spectrometer. The mass spectrometric studies were conducted using a Voyager DE PRO Biospectrometry Workstation (Applied Biosystems) MALDI-TOF MS instrument. A pulsed nitrogen laser of 337 nm was used (maximum firing rate, 20 Hz; maximum pulse energy: 300 μ J) for desorption ionization and TOF was operated in the delayed extraction mode. For the mass spectrometric study, W + Se and W + S systems were dispersed in acetone and directly spotted on the target plate. The sample was dried in ambience and inserted into the spectrometer. Typical delay times employed were of the order of 75–100 ns. The mass spectra were collected in the anion mode and were averaged for 100 shots. No magic ion formation was observed in the positive ion mode. Most of the measurements were done in the linear TOF mode.

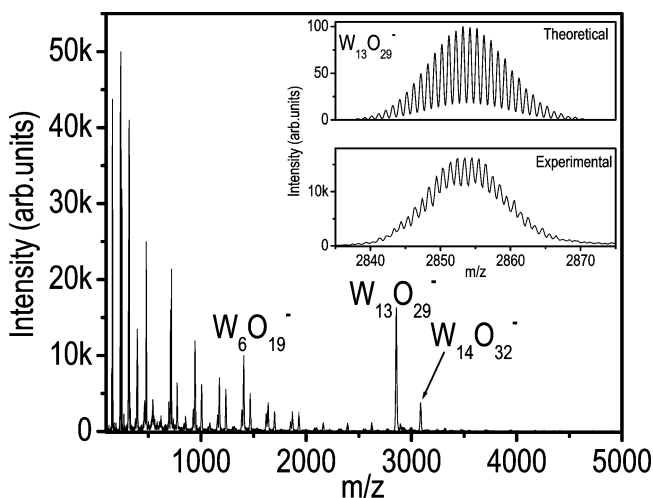


Figure 1. LDI mass spectrum of W + Se mixture in the negative ion mode, showing $W_{13}O_{29}^-$ and $W_{14}O_{32}^-$ clusters. Inset shows an expanded view of the $W_{13}O_{29}^-$ region, showing the isotope distribution, which matches exactly with the theoretical pattern.

The magic cluster peaks were significantly higher in intensity when white dispersion of WO was used, which was obtained by sonicating a well-ground Mo + Se sample in acetone for 10 min. A white dispersion was directly spotted on the target plate, giving a white powder film upon drying (the sample turned out to be WO_x from analyses, described in detail below), and LDI mass spectra were taken from the film. This white powdered material, obtained by evaporation of the solvent in the dispersion, was used for various spectroscopic, microscopic, and diffraction studies using standard instrumentation. Raman spectra were measured using Witec GmbH confocal Raman spectrometer equipped with a 532 nm laser. Scanning electron microscopy (SEM) and energy dispersive analysis of X-rays (EDAX) were done with a FEI QUANTA 200 instrument. X-ray photoelectron spectroscopy (XPS) measurements were done using an Omicron Nanotechnology spectrometer with polychromatic Al K α X-rays. Binding energy (BE) was calibrated with respect to C1s at 285.0 eV.

3. Computational Methods

The relativistic quantum chemical computations were performed to understand the electronic structures and the relative

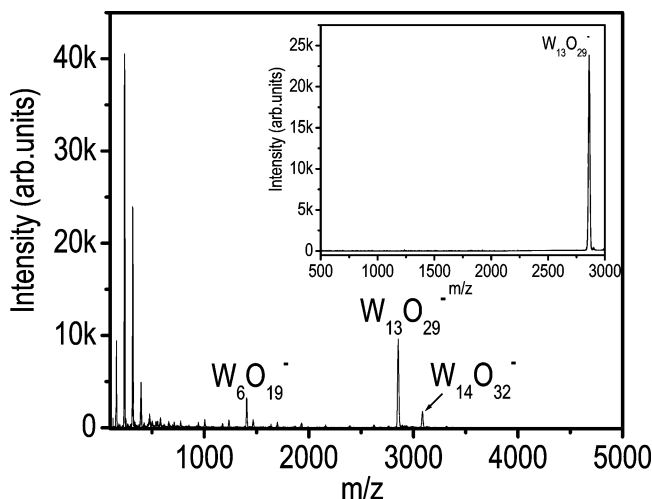


Figure 2. Negative mode LDI mass spectrum of white dispersion showing $W_6O_{19}^-$, $W_{13}O_{29}^-$, and $W_{14}O_{32}^-$. Inset: PSD mode LDI mass spectrum of $W_{13}O_{29}^-$ showing no fragmentation.

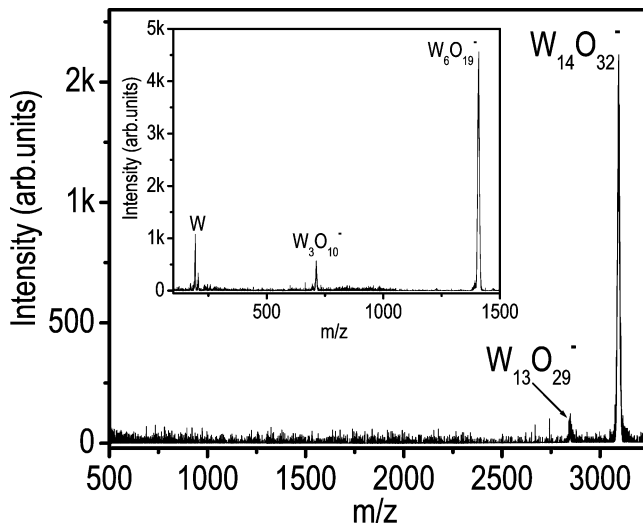


Figure 3. PSD mode LDI mass spectrum of $W_{14}O_{32}^-$ showing fragment at $W_{13}O_{29}^-$. Inset shows the PSD mode LDI mass spectrum of $W_6O_{19}^-$ showing fragments at $W_3O_{10}^-$ and W^- .

stability of experimentally observed magic-number clusters in the gas phase. The density functional theory (DFT)²⁵ method was used together with relativistic effective core potentials (RECPs) for the W atoms. The initial geometry of $W_6O_{19}^{2-}$ was taken from the available crystal data.²⁶ The $W_{13}O_{29}^-$ and $W_{14}O_{32}^-$ geometries are modeled from the Keggin structures.²⁷ Keggin structures are best-known starting geometry for the heteropolyanions. The geometries of WO clusters such as $W_6O_{19}^{2-}$, $W_{13}O_{29}^-$, and $W_{14}O_{32}^-$ in the gas phase were optimized using the DFT. The DFT approach utilized Becke's three-parameter functional and local correlation and nonlocal functional (abbreviated as B3LYP).^{28–30} All the calculations were carried out using RECPs, which represent the effect of the core electrons of tungsten in WO clusters. Los Alamos National Laboratory (LANL) effective core potential was combined with B3LYP method to account for the core electrons of tungsten atom. The double- ζ (DZ) valence basis set and the

combination of ECP is thus referred to as "LANL2DZ" basis,^{31–33} which was used for geometry optimization. The vibrational frequency computations were performed to confirm the equilibrium geometries, which are really in true minima. All computations were performed using the G03 package.³⁴ We have also obtained the electron density plots of all the tungsten clusters using the Molden software.³⁵

4. Results and Discussion

Although we expected gas phase tungsten sulphide and tungsten selenide clusters from W + S and W + Se mixtures, respectively, the results showed the formation of tungsten oxide clusters, with some magic peaks (Figure 1). While investigating every peak in greater detail, we found that WO_3 was the precursor leading to the formation of the clusters. Clusters with general formula, $(W_nO_{3n})O^-$, where $n = 1$ to 8 were clearly

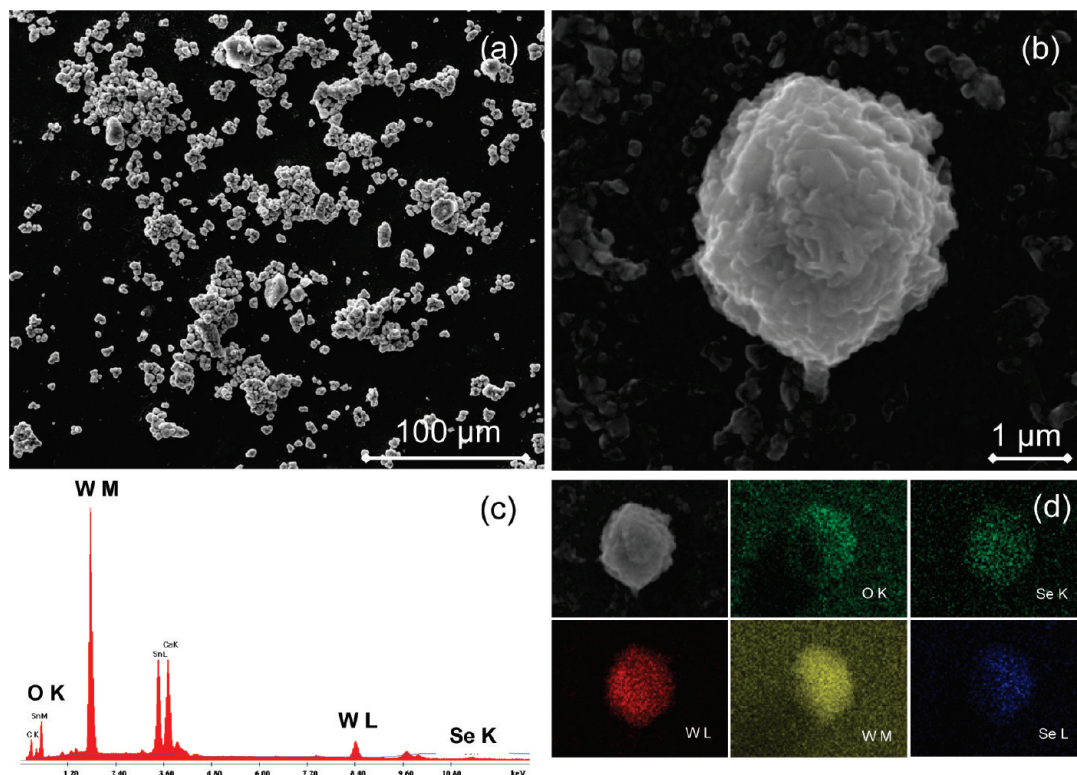


Figure 4. SEM images of the white dispersion. (a) Large area image, (b) magnified image of a single particle, (c) EDAX spectrum of b, and (d) corresponding elemental maps in the W, O, and Se regions. The Sn and Ca peaks are due to the substrate.

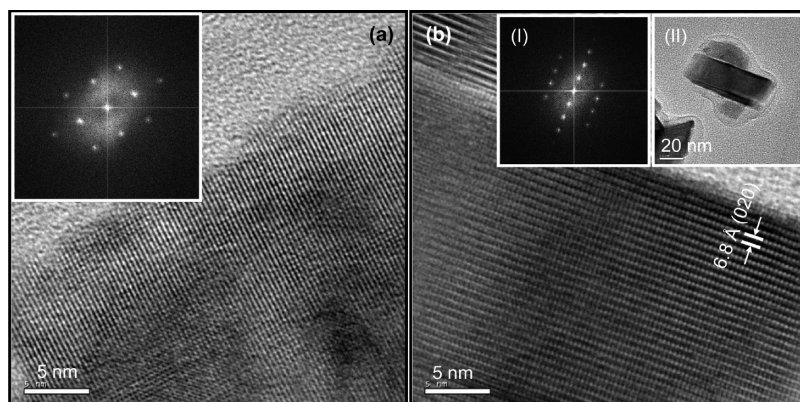


Figure 5. (a) HRTEM image of the white dispersion showing a lattice spacing of 3.8 Å corresponding to the (001) plane of WO_3 .³⁶ Inset: Fourier transform of the image showing cubic ordering. (b) Lattice image of the white dispersion showing spacing of 6.8 Å, possibly due to the (020) plane of WO_3 .³⁷ Inset: (I) Fourier transform of the image showing an elongated c -axis structure and (II) large area image of a single particle from the white dispersion.

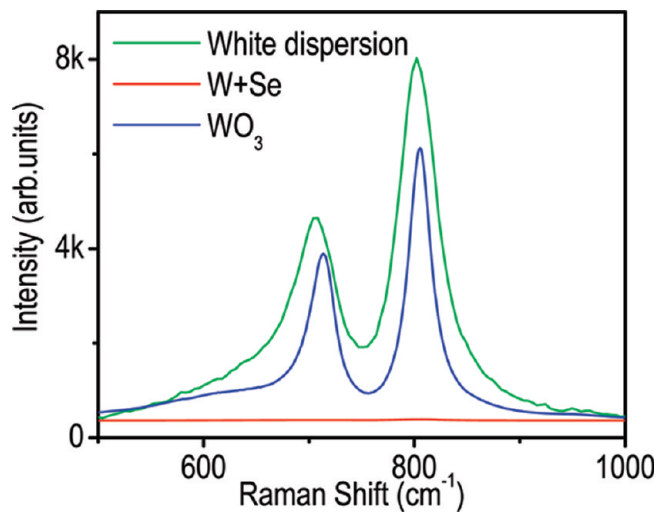


Figure 6. Overlaid Raman spectra of nano tungsten oxide, bulk WO_3 , and $\text{W} + \text{Se}$, collected with 532 nm excitation.

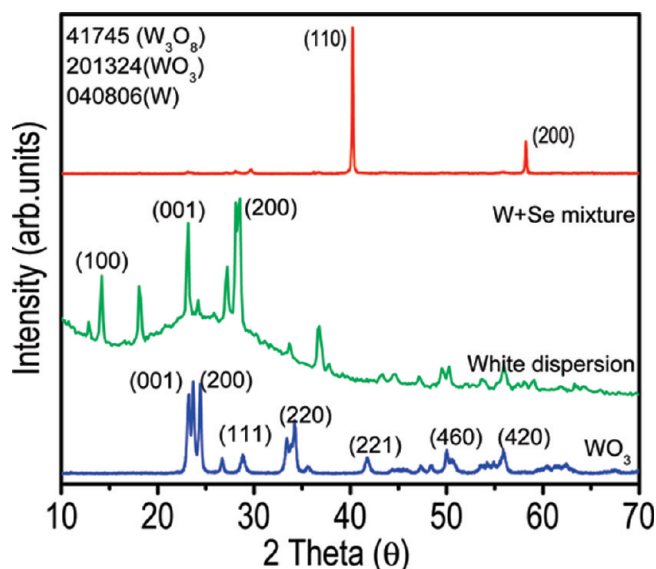


Figure 7. Overlaid X-ray diffraction patterns for nano tungsten oxide, bulk WO_3 and $\text{W} + \text{Se}$. The reflections labeled on the pattern of white dispersion are due to W_3O_8 .

observed in view of their characteristic isotope pattern, suggested that such compositions are stable and abundant. Apart from the general formula, some other clusters were also observed, namely, Se_2^- , Se_3^- , Se_4^- , Se_5^- , $\text{W}_4\text{O}_{17}^-$, $\text{W}_5\text{O}_{20}^-$, $\text{W}_6\text{O}_{23}^-$, $\text{W}_7\text{O}_{26}^-$, $\text{W}_8\text{O}_{26}^-$, etc. Beyond this mass region, some changeover in the pattern of cluster formation occurred and thereafter the peaks were not conforming to a general formula. The peaks with the general formula, $(\text{W}_n\text{O}_{3n})\text{O}^-$ vanished and a new set of peaks started to appear. In that region, interestingly, a peak with mass exactly matching with the formula, $\text{W}_{13}\text{O}_{29}^-$ appeared with high intensity suggesting enhanced stability for it over the neighboring peaks. The intense W_{13} peak was found in $\text{W} + \text{Se}$ mixture as well as in the $\text{W} + \text{S}$ mixture. In both the spectra, the intensity of the magic-numbered peak was higher than the neighboring clusters. These clusters cannot be composed of W and Se . The W isotope pattern was clearly discernible in all the clusters and a comparison of the theoretical and observed pattern was used to assign the peaks.

While comparing $\text{W} + \text{Se}$ and $\text{W} + \text{S}$ mixtures, the $\text{W} + \text{Se}$ mixture showed good intensity for the W_{13} cluster. Figure 1 shows it clearly for the $\text{W} + \text{Se}$ mixture. The isotope pattern

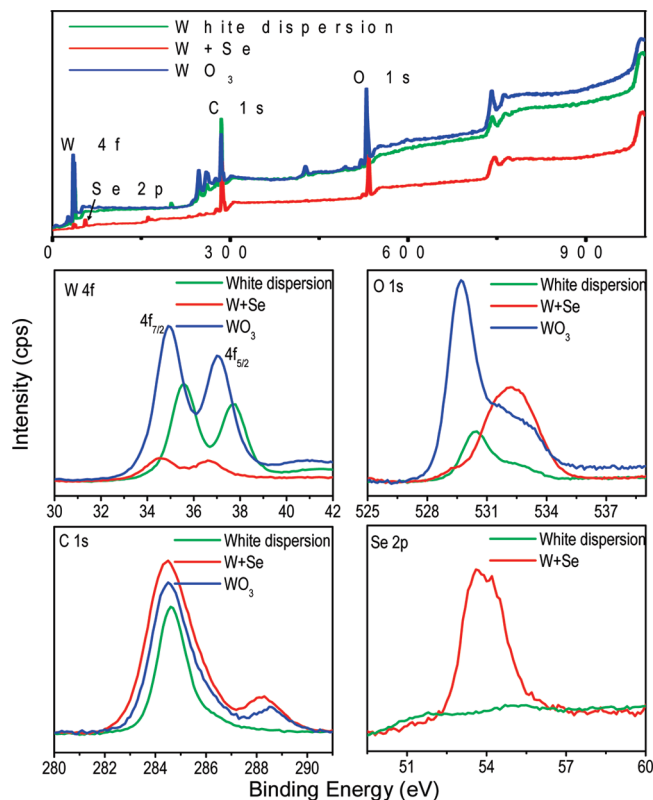


Figure 8. Overlaid XPS spectra for white dispersion, $\text{W} + \text{Se}$ and bulk WO_3 .

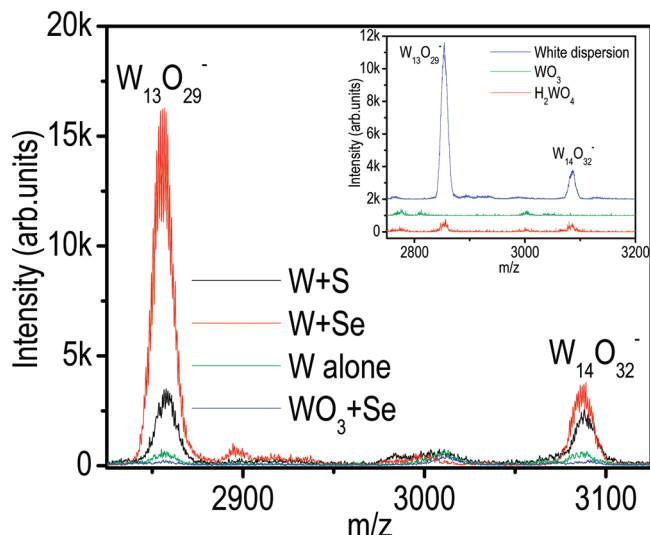


Figure 9. Overlaid LDI spectra of $\text{W} + \text{S}$, $\text{W} + \text{Se}$, W alone, and $\text{WO}_3 + \text{Se}$ in negative ion mode showing $\text{W}-\text{O}$ magic cluster ions. Inset shows the comparison of nano tungsten oxide with WO_3 and H_2WO_4 .

matched perfectly. A similar cluster, $\text{W}_{14}\text{O}_{32}^-$ was also observed. Beyond these peaks, the mass spectra did not reveal any interesting ions.

Relative intensities of the magic cluster peaks $\text{W}_6\text{O}_{19}^-$, $\text{W}_{13}\text{O}_{29}^-$, and $\text{W}_{14}\text{O}_{32}^-$ were significantly high compared to the neighboring clusters, when a milky white dispersion was used. A typical spectrum is shown in Figure 2.

Stability of the ions was validated using the PSD data. The PSD spectrum of $\text{W}_{13}\text{O}_{29}^-$ did not show any fragmentation, as shown in the inset to Figure 2, even at the highest laser power. $\text{W}_6\text{O}_{10}^-$ and $\text{W}_{14}\text{O}_{32}^-$ exhibited fragmentation as shown in

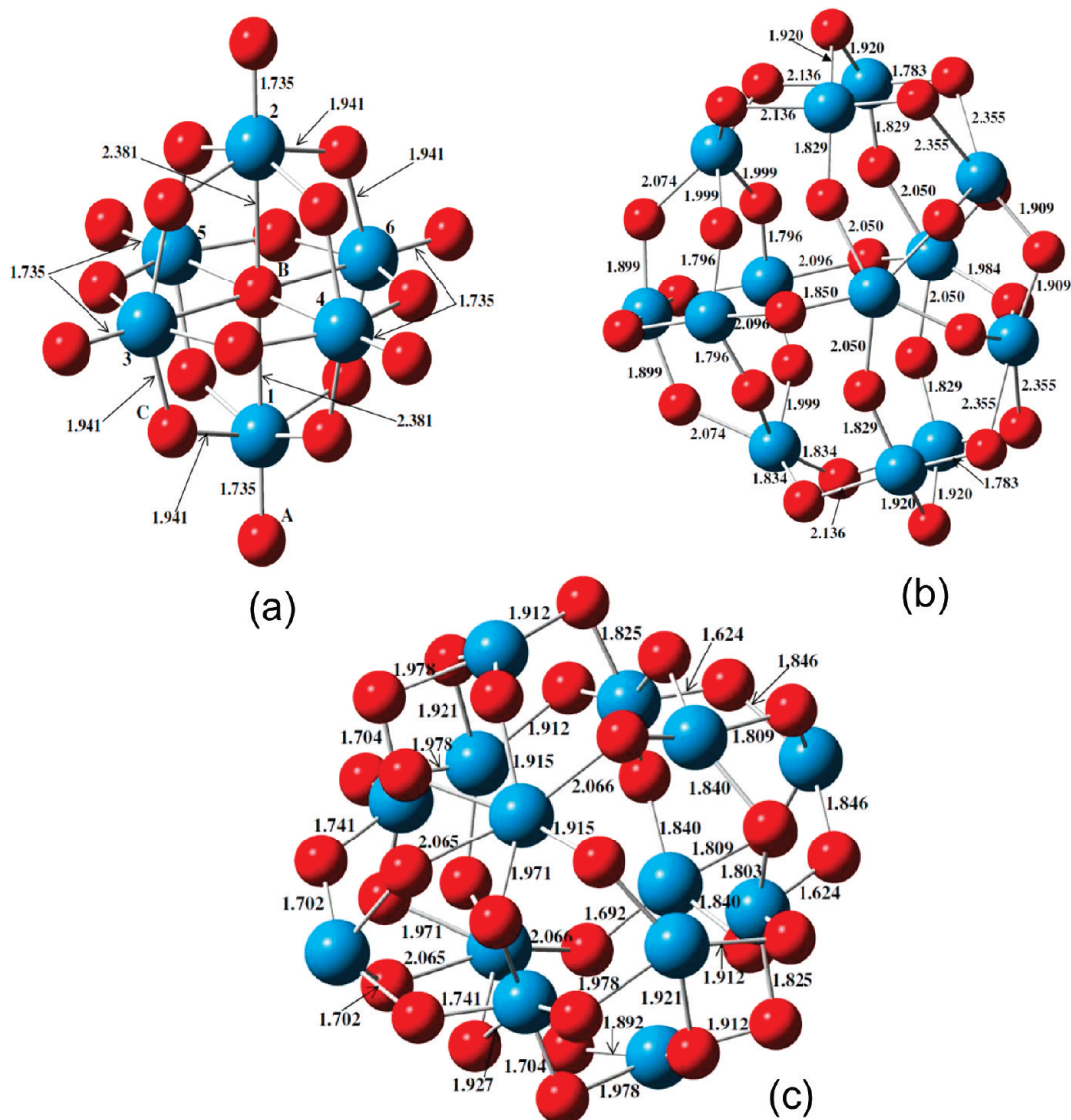


Figure 10. The structure of tungsten clusters in gas phase at B3LYP/LANL2DZ level of theory (a) $W_6O_{19}^{2-}$, (b) $W_{15}O_{29}^-$, (c) $W_{14}O_{32}^-$. Tungsten and oxygen atoms are represented by blue and red balls, respectively.

Figure 3. $W_{14}O_{32}^-$ on fragmentation showed $W_{13}O_{29}^-$, while $W_6O_{19}^-$ gave fragments such as $W_3O_{10}^-$ and W^- .

The milky white material was analyzed using SEM, EDAX, transmission electron microscopy (TEM), XPS and Raman spectroscopy. These investigations were done to characterize the nature of the starting material used for LDI. Figure 4 shows the detailed SEM analysis with a large area image and that of a single agglomerate having several nanoflakes of tungsten oxide. Elemental mapping and EDAX analysis confirmed the formation of the oxide. Incorporation of Se was also noted.

Figure 5 shows the HRTEM data of the white material. From the images, it was confirmed that the material formed is nanoscale tungsten oxide. The HRTEM analysis supports the formation of multiple tungsten oxide phases. In certain regions, a cubic ordering is seen, but there are also other regions in which a longer axis is observed. Thus the white dispersion appears to be a mixture of cubic WO_3 and orthorhombic W_3O_8 . The results were compared with the data of bulk tungsten oxide (see below).

Raman analysis shows typical bands corresponding to WO_3 , as reported in the literature. Major peaks at 703 and 802 cm^{-1} were characteristic O–W–O vibrations.³⁸ The peak at 703 cm^{-1} corresponds to the bending mode of O–W–O and 802 cm^{-1} corresponds to the stretching mode of O–W–O. Figure

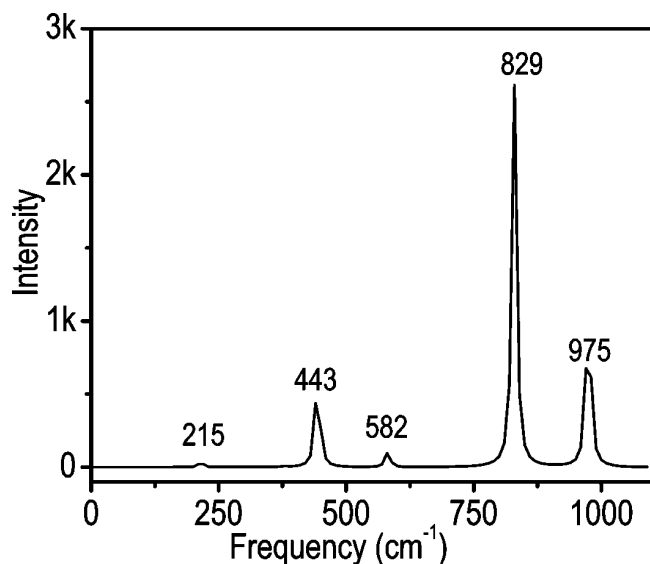
6 shows the Raman spectrum of the white dispersion. Raman spectral analysis showed that the formed nano tungsten oxide is similar to bulk WO_3 with little shift in peak position.

Figure 7 shows the overlaid X-ray diffraction patterns. XRD results were also compared with that of bulk WO_3 . The XRD pattern of white dispersion was not matching exactly with WO_3 pattern, although some of the peaks of the latter were seen. A few lines could be indexed to the intense reflections of W_3O_8 . This shows that the white dispersion may be a mixture of different phases of tungsten oxide such as cubic WO_3 and orthorhombic W_3O_8 . The XRD peaks have been assigned with the help of JCPDS database files 201324 (WO_3), 41745 (W_3O_8), and 040806 (W).

XPS analysis also reveals the formation of a tungsten oxide phase in the white dispersion. This was not apparent in the sample in which tungsten and selenium powders were mixed without grinding and sonication. Figure 8 shows the overlaid XPS spectra of nano tungsten oxide, W+Se mixture and bulk WO_3 . All the expected elements are present in the survey scans. A higher binding energy for W 4f in the white dispersion compared to bulk WO_3 clearly indicates the formation of the material in the nanoscale. The oxides show higher binding energy for W 4f, as expected. The O 1s is similar in all cases,

TABLE 1: The Structural Parameters of $W_6O_{19}^{2-}$ in Gas Phase The Numbering and Labeling followed are as shown in Figure 10a

structural parameters	$W_6O_{19}^{2-}$	
	B3LYP/LANL2DZ	crystal data ^a
bond distance (Å)		
W_n-O_A ($n = 1$ to 6)	1.735	1.718
W_n-O_B ($n = 1$ to 6)	2.381	2.319–2.329
W_n-O_C ($n = 1$ to 6)	1.941	1.897–1.944
bond angle (degree)		
$O_A-W_n-O_C$ ($n = 1$ to 6)	105.0–105.2	102.4–104.7
$O_A-W_n-O_B$ ($n = 1$ to 6)	180.0	178.4–179.1
$W_1-O_B-W_2$	180.0	180.0
$W_3-O_B-W_6$	180.0	180.0
$W_4-O_B-W_5$	180.0	180.0
$W_3-O_B-W_4$	90.0	89.9
$W_3-O_B-W_5$	90.0	90.1
$W_4-O_B-W_6$	90.0	90.1
$W_5-O_B-W_6$	90.0	89.9
$W_n-O_C-W_n$	120.2	116.9–118.8
$O_C-W_n-O_C$ ($n = 1$ to 6)	86.1	85.1–88.3
$O_C-W_n-O_C$ ($n = 1$ to 6)	149.8	151.4–152.8
dihedral angle (degree)		
$O_A-W_1-O_B-W_2$	180.0	180.0
$O_A-W_2-O_B-W_1$	180.0	180.0
$O_A-W_n-O_C-W_n$	–179.9	–177.9 to –179.7
$O_A-W_n-O_C-W_n$	179.9	177.–179.9
$W_n-O_C-W_n-O_C$	–75.4	–78.1 to –78.4
$W_n-O_C-W_n-O_C$	75.4	74.1–78.4
$W_n-O_C-W_n-O_C$	–0.04	–1.2 to –2.2
$W_n-O_C-W_n-O_C$	0.1	1.3–5.5

^a From ref 22.**Figure 11.** The infrared spectrum of $W_6O_{19}^{2-}$ clusters in the gas phase. The frequencies (cm^{-1}) are computed in the gas phase at B3LYP/LANL2DZ level of theory.

with a lower BE for the bulk, than the nanoscale material. The W+Se mixture shows the highest BE, possibly due to adsorbed oxygen species. All the materials showed adventitious carbon.

The formation of W_{13} cluster from other sources like WO_3 -Se and W alone was also explored. These results were compared with LDI of WO_3 and H_2WO_4 . W_{13} magic cluster was expected from WO_3 and H_2WO_4 but in both the cases, there was no ion of this composition with unusual intensity. Selenium addition was thought to give magic clusters with WO_3 , but that too failed to generate the cluster in question. In Figure 9, all

the spectra obtained from the above experiments are overlaid. From these results, it is clear that W + Se and W + S mixtures only generate W_{13} cluster. While comparing Se and S, Se is found to be a better candidate to form W_{13} clusters. It is possible that the oxidizing behavior of selenium aids in the formation of the oxide at the metal surface. Nanoscale oxides at the surface may form clusters upon laser desorption. Interestingly, selenium addition enhances the desorption and ionization. It appears that thinner flakes are easier to get desorbed that could be curling to form cage-like structures in the gas phase.

The computed geometry of $W_6O_{19}^{2-}$ as shown in Figure 10a reveals that each tungsten atom is bonded with six oxygen atoms. Three different types of W–O bond distances are observed at 1.735, 1.941, and 2.381 Å, respectively. This is a consequence of the existence of three types of W atoms with each type of W atom exhibiting a unique set of distances with its surrounding oxygen atoms. The structural parameters of $W_6O_{19}^{2-}$ at B3LYP/LANL2DZ level of theory are compared with available crystal geometry²² in Table 1. Our optimized geometrical parameters compare well with crystal structure suggesting that the tungsten cluster optimization is fairly accurate to derive the structural and thermodynamic parameters. The infrared spectrum of $W_6O_{19}^{2-}$ is shown in Figure 11. The vibrational frequencies of $W_6O_{19}^{2-}$ cluster are computed at B3LYP/LANL2DZ level of theory. Five vibrational modes are observed at frequencies in the range of 100 to 1100 cm^{-1} . The frequencies at 975 and 215 cm^{-1} correspond to the symmetric stretching and bending mode of W– O_A vibrations, respectively. The peaks at 829 and 443 cm^{-1} correspond to the symmetric stretching and bending stretching modes of O_C –W– O_C vibrations, respectively. The symmetric stretching mode of O_C – O_B – O_C appears at 582 cm^{-1} . The Laplacian density plot of $W_6O_{19}^{2-}$ is shown in Figure 12a. The density plot clearly reveals the delocalization of the anionic electron density over three inequivalent subunits of W–O cluster moieties of the $W_6O_{19}^{2-}$ system.

The optimized equilibrium structure of $W_{13}O_{29}^-$ is shown in Figure 10b. The structural parameters, as shown in Figure 10b, indicate that the bond distances are unique for each W atom with its surrounding oxygen atoms. The Laplacian density of $W_{13}O_{29}^-$ is shown in Figure 12b. The density plot of $W_{13}O_{29}^-$ reveals delocalization of the anionic charges over the various subunits of the $W_{13}O_{29}^-$ cluster. The geometry of $W_{14}O_{32}^-$ is shown in Figure 10c. The $W_{14}O_{32}^-$ structural parameters are consistent with those of $W_6O_{19}^{2-}$ and $W_{13}O_{29}^-$ clusters. The Cartesian coordinates of the atoms of $W_6O_{19}^{2-}$, $W_{13}O_{29}^-$, and $W_{14}O_{32}^-$ clusters are given in Supporting Information Table S1, Table S2, and Table S3, respectively. The Cartesian coordinates of $W_6O_{19}^{2-}$, $W_{13}O_{29}^-$, and $W_{14}O_{32}^-$ clusters are provided as supporting materials. The Laplacian density of $W_{14}O_{32}^-$ cluster as shown in Figure 12 (c) shows the similar features as observed in the case of $W_{13}O_{29}^-$ cluster. All of these charge density profiles reveal (1) delocalization of the anionic charges (2) strong W^+O^- ionic characters as demonstrated by the Laplacians of charge densities. The unusual stabilities of the magic number clusters are thus attributed to the optimal delocalization of the anionic electronic charge among various W–O oxide subunits present in the cluster.

The atomization energies per atom of WO , $W_6O_{19}^{2-}$, $W_{13}O_{29}^-$, and $W_{14}O_{32}^-$ are given in the Table 2 together with the total atomization energies. The atomization energy (AE) is calculated as the difference between the total electronic energy of the optimized cluster at its equilibrium geometry and the total energy of individual atoms. As can be seen from Table 2, the

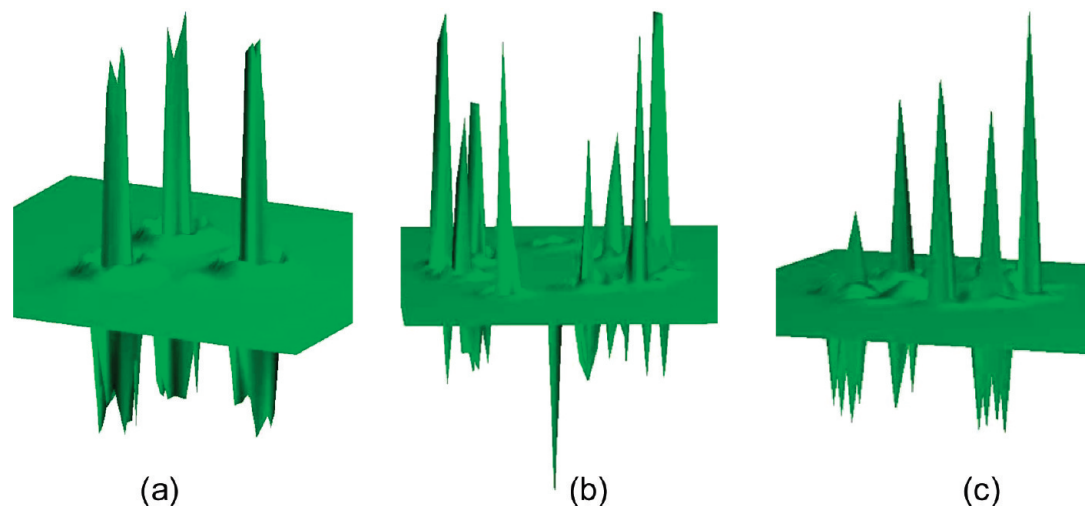


Figure 12. Laplacian density of tungsten clusters in gas phase at B3LYP/LANL2DZ level of theory (a) $W_6O_{19}^{2-}$, (b) $W_{13}O_{29}^{2-}$, (c) $W_{14}O_{32}^{2-}$.

TABLE 2: Atomization Energy of Tungsten Clusters in Gas Phase at B3LYP/LANL2DZ Level of Theory^a

clusters	atomization energy (eV)	atomization energy per atom (eV)
WO	6.612	3.306
$W_6O_{19}^{2-}$ ^b	144.036	5.761
$W_{13}O_{29}^{2-}$	219.962	5.237
$W_{14}O_{32}^{2-}$	177.781	3.865

^a The atomization energy is calculated as the individual of $W^0 + O + O^-$ atoms. ^b The total energy of individual of $W^0 + O + O^{2-}$ atoms show better stability in the atomization energy per atom as 6.242 eV.

atomization energy per atom clearly reveals that the magic-number clusters are unusually stable as they exhibit greater AE/atom. In the case of $W_6O_{19}^{2-}$ cluster, the AE relative to $W^0 + O + O^{2-}$ (6.242 eV) is higher compared to $W^0 + O + O^-$ atoms (5.761 eV). Our theoretical results compare well with the experimental observations. The computed stabilities are also consistent with the nonobservation of fragmentation patterns for the magic number clusters.

5. Conclusion

Closed-cage clusters of composition, $W_6O_{19}^{2-}$, $W_{13}O_{29}^{2-}$, and $W_{14}O_{32}^{2-}$ were detected in the laser desorption mass spectra of W–Se and W–S mixtures. Further study of the precursor revealed the formation of nano tungsten oxide from a mixture of W and Se. Our relativistic quantum chemical computations revealed the structure and stabilities of W_6 , W_{13} , and W_{14} clusters. The computed atomization energies are consistent with the LDI mass spectra of these clusters that also supports the observed stability of these clusters. Clusters of this kind composed of tungsten and oxygen are reported for the first time in the gas phase. The presence of prominent peaks for $W_6O_{19}^{2-}$, $W_{13}O_{29}^{2-}$, and $W_{14}O_{32}^{2-}$, especially for these compositions is supported by the computed atomization energies of these clusters which reveal enhanced stabilities for these compositions. Structure and stability of these unique magic numbered clusters will be of great interest, especially for their catalytic applications. The reactivity in the gas phase can be studied by trapping the clusters and reaction intermediates using 3D trap mass spectrometers. Gas phase structural analysis is feasible with ion mobility experiments, to confirm the proposed structures.

Acknowledgment. The nanomaterials program at IIT, Madras is supported by the Department of Science and Technology.

D.M.D.J.S. was supported by a Swarnajayanti Fellowship awarded to T.P. The work at Cal State was supported by the U.S. Department of Energy under Grant DE-FG2-05ER15657. The work at LLNL was performed under the auspices of U.S. Department of Energy under Contract No. W-7405-Eng-48.

Supporting Information Available: The Cartesian coordinates of the atoms of $W_6O_{19}^{2-}$, $W_{13}O_{29}^{2-}$, and $W_{14}O_{32}^{2-}$ cluster at B3LYP/LANL2DZ level of theory. This material is available free of charge via the Internet at <http://pubs.acs.org>.

References and Notes

- (1) Shang, M. H.; Wei, S. H.; Zhu, Y. J. *J. Phys. Chem. C* **2009**, *113*, 15507.
- (2) Zhou, X.; Wu, M. M.; Zhou, J.; Sun, Q. *Appl. Phys. Lett.* **2009**, *94*, 103105.
- (3) Castleman, A. W., Jr.; Khanna, S. N. *J. Phys. Chem. C* **2009**, *113*, 2664.
- (4) Maruyama, S.; Kohno, M.; Inoue, S. *Therm. Sci. and Eng.* **1999**, *7*, 69.
- (5) Bergeron, D. E.; Castleman, A. W., Jr.; Morisato, T.; Khanna, S. N. *Science* **2004**, *304*, 84.
- (6) Roach, P. J.; Woodward, W. H.; Castleman, A. W., Jr.; Reber, A. C.; Khanna, S. N. *Science* **2009**, *323*, 492.
- (7) Kéki, S.; Szilagy, L. S.; Torok, J.; Deak, G.; Zsuga, M. *J. Phys. Chem. B* **2003**, *107*, 4818.
- (8) Kéki, S.; Nagy, L.; Deák, G.; Zsuga, M. *J. Am. Soc. Mass Spectrom.* **2004**, *15*, 1455.
- (9) Aubriet, F.; Muller, J. F. *J. Phys. Chem. A* **2002**, *106*, 6053.
- (10) Maleknia, S.; Brodbelt, J.; Pope, K. *J. Am. Soc. Mass Spectrom.* **1991**, *2*, 212.
- (11) Faggiani, R.; Gillespie, R. J.; Vekris, J. E. *J. Chem. Soc., Chem. Commun.* **1988**, 902.
- (12) Asmis, K. R.; Sauer, J. *Mass Spectrom. Rev.* **2007**, *26*, 542.
- (13) Searcy, J. Q.; Fenn, J. B. *J. Chem. Phys.* **1974**, *61*, 5282.
- (14) Yang, C. L.; Wang, M. S.; Sun, M. Y.; Wang, D. H.; Ma, X. G.; Gong, Y. B. *Chem. Phys. Lett.* **2008**, *457*, 49.
- (15) Ide, Y.; Shibahara, T. *Inorg. Chem. Commun.* **2004**, *7*, 1132.
- (16) Bridgeman, J.; Cavigliasso, G. *J. Phys. Chem. A* **2002**, *106*, 6114.
- (17) Guo, B. C.; Kerns, K. P.; Castleman, A. W., Jr. *Science*, **1992**, *255*, 1411.
- (18) Johnson, G. E.; Tyo, E. C.; Castleman, A. W., Jr. *Proc. Natl. Acad. Sci. U.S.A.* **2008**, *105*, 18108.
- (19) Rothgeb, D. W.; Hossain, E.; Kuo, A. T.; Troyer, J. L.; Jarrold, C. C.; Mayhall, N. J.; Raghavachari, K. *J. Chem. Phys.* **2009**, *130*, 124314.
- (20) Singh, D. M. D. J.; Pradeep, T.; Bhattacharjee, J.; Waghmare, U. V. *J. Phys. Chem. A* **2005**, *109*, 7339.
- (21) Singh, D. M. D. J.; Pradeep, T.; Bhattacharjee, J.; Waghmare, U. V. *J. Am. Soc. Mass Spectrom.* **2007**, *18*, 2191.
- (22) Singh, D. M. D. J.; Pradeep, T. *Chem. Phys. Lett.* **2004**, *395*, 351.
- (23) Singh, D. M. D. J.; Pradeep, T. *Chem. Phys. Lett.* **2006**, *417*, 34.
- (24) Kroto, H. W.; Heath, J. R.; O'Brien, S. C.; Curl, R. F.; Smalley, R. E. *Nature* **1985**, *318*, 162.

- (25) Parr, R. G.; Yang, W. *Density Functional Theory of Atoms and Molecules*; Oxford: New York, 1989.
- (26) Parvez, M.; Boorman, M. P.; Langdon, N. *Acta Cryst. C* **1998**, *54*, 608.
- (27) Keggin, J. F. *Proc. R. Soc. London, Ser. A* **1934**, *144*, 75.
- (28) Becke, A. D. *J. Chem. Phys.* **1993**, *98*, 5648.
- (29) Vosko, S. H.; Wilk, L.; Nusair, M. *Can. J. Phys* **1980**, *58*, 1200.
- (30) Lee, T.; Yang, W. T.; Parr, R. G. *Phys. Rev. B* **1988**, *37*, 785.
- (31) Hay, P. J.; Wadt, W. R. *J. Chem. Phys.* **1985**, *82*, 270.
- (32) Wadt, W. R.; Hay, P. J. *J. Chem. Phys.* **1985**, *82*, 284.
- (33) Hay, P. J.; Wadt, W. R. *J. Chem. Phys.* **1985**, *82*, 299.
- (34) Frisch, M. J.; et al. *Gaussian 03*, revision C.02; Gaussian, Inc.: Pittsburgh, PA, 2005.
- (35) Schaftenaar, G.; Noordik, J. H. *J. Comput.-Aided Mol. Des* **2000**, *14*, 123.
- (36) Deepa, M.; Srivastava, A. K.; Kar, M.; Agnihotry, S. A. *J. Phys. D: Appl. Phys.* **2006**, *39*, 1885.
- (37) Doucette, L. D.; Santiago, F.; Moran, S. L.; Lad, R. J. *J. Mater. Res.* **2003**, *18*, 2859.
- (38) Szilágyi, I. M.; Wang, L.; Gouma, P. I.; Balázsi, C.; Madarász, J.; Pokol, G. *Mater. Res. Bull.* **2009**, *44*, 505.

JP911922A